

To β or not to β : can higher-order Jeans analysis break the mass–anisotropy degeneracy in simulated dwarfs?

A. Genina^{1*}, J. I. Read², C. S. Frenk¹, S. Cole¹, A. Benítez-Llambay¹,
A. D. Ludlow³, J. F. Navarro^{4†}, K. A. Oman¹, A. Robertson¹

¹ *Institute for Computational Cosmology, Department of Physics, Durham University, South Road, Durham DH1 3LE, UK*

² *Department of Physics, University of Surrey, Guildford, GU2 7XH, UK*

³ *International Centre for Radio Astronomy Research, University of Western Australia, 35 Stirling Highway, Crawley, Western Australia, 6009, Australia*

⁴ *Department of Physics & Astronomy, University of Victoria, Victoria, BC, V8P 5C2, Canada*

Accepted XXX. Received YYY; in original form ZZZ

ABSTRACT

A non-parametric higher-order Jeans analysis method, GRAVSPHERE, was recently used to constrain the density profiles of Local Group dwarf galaxies, classifying them into those that are more likely to have an inner dark matter cusp and those that are likely to have a core (Read et al.). In this work we test this method using 31 simulated galaxies, comparable to Fornax, selected from the APOSTLE suite of cosmological hydrodynamics simulations, which include CDM and Self-Interacting Dark Matter (SIDM) cosmologies. We find that the mass profiles of the simulated dwarfs are often, but not always, well recovered by GRAVSPHERE. The less successful cases may be identified using a χ^2 diagnostic. Although the uncertainties are large in the inner regions, the inferred mass profiles are unbiased and exhibit smaller scatter than comparable Jeans methods. We find that GRAVSPHERE recovers the density profiles of simulated dwarfs below the half-light radius and down to the resolution limit of our simulations with better than 10(\pm 30) per cent accuracy, making it a promising Jeans-based approach for modelling dark matter distributions in dwarf galaxies.

Key words: galaxies: dark matter – galaxies: dwarf – galaxies: kinematics and dynamics

1 INTRODUCTION

Dark matter makes up ~ 85 per cent of the matter density of the Universe (e.g. Planck Collaboration et al. 2018), yet its nature remains unknown. Dwarf satellite galaxies of the Milky Way are expected to be excellent laboratories for testing the properties of dark matter (Battaglia et al. 2013). These objects have velocity dispersions indicative of a high dark matter content. If dark matter is a self-annihilating particle, the products of its annihilation may be detected with space and ground-based instruments (Lake 1990), such as Fermi-LAT (Albert et al. 2017) and the upcoming Cherenkov Telescope Array (Morselli & Consortium 2017). The detected spectra of these annihilation products would reveal the particle physics properties of dark matter; however, these analyses require the underlying dark matter distribution to be well constrained. Some of the classical dSphs, like Sculptor and Fornax, host $\sim 10^6$ – $10^8 M_{\odot}$ in stars

(McConnachie 2012) and are sufficiently close to our Galaxy that large samples of high-quality kinematic and photometric data can be obtained, so inferences may be made of the underlying gravitational potential (e.g. Battaglia et al. 2008; Strigari et al. 2008; Walker et al. 2009; Gaskins 2016; Strigari 2018; Charbonnier et al. 2011; Bonnivard et al. 2015b; Read et al. 2019).

The exact dark matter density distribution in the central regions of dwarf galaxies has been controversial (e.g. de Blok 2010). Galaxy rotation curves measured in some dwarf irregulars (Moore 1994; Oh et al. 2008; Zhu et al. 2016; Adams et al. 2014; Oh et al. 2015; Read et al. 2017), analyses based on multiple tracer populations in dwarf spheroidals (Walker & Peñarrubia 2011) and globular cluster survivability within dwarfs (Goerdt et al. 2006; Cole et al. 2012; Contenta et al. 2018; Orkney et al. 2019) have been used to argue in favour of dark matter “cores”, where the density remains constant in the central regions, with $\rho \propto r^0$ (Flores & Primack 1994; Moore 1994). On the other hand, dark matter-only N -body simulations in Λ CDM cosmologies have

* E-mail: anna.genina@durham.ac.uk (AG)

† Senior CIFAR Fellow (JFN)

found “cusps” in inner haloes, with density profiles scaling approximately as $\rho \propto r^{-1}$ (Navarro et al. 1997, 1996b). This became known as the “core-cusp problem”. The problem has motivated the introduction of alternative dark matter models, such as self-interacting dark matter, where cores are created through dark matter self-scattering on a scale related to the interaction cross-section (Spergel & Steinhardt 2000; Elbert et al. 2015).

In recent years, the use of hydrodynamics to model baryonic processes have become more common in simulations. Outflows associated with supernova feedback have been shown to cause fluctuations in the gravitational potential, which can alter the inner structure of haloes. This may occur in a single violent burst (Navarro et al. 1996a) or through repeated dark matter “heating” over time (Read & Gilmore 2005; Pontzen & Governato 2012; Oñorbe et al. 2015; Read et al. 2016). Cores in these model typically form on the scale of the half-light radius of dwarf galaxies.

The formation of cores in dwarfs that have undergone extended periods of star formation is a testable hypothesis. This idea was explored in Read et al. (2019). These authors find that dSphs which have continued to form stars until recent times, like Fornax and the Local Group dIrrs, have lower densities at 150 pc, ρ_{150} , than those predicted for isolated dwarfs using the mass-concentration relation in Λ CDM (Dutton & Macciò 2014). These lower densities could be explained by core formation through dark matter heating. The dwarfs that have ceased star formation a long time ago have values of ρ_{150} , consistent with a cusp.

Read et al. (2019) used Jeans analysis applied to line-of-sight stellar velocities and projected positions to place constraints on the dark matter density distribution of the gas-free dwarf spheroidals. This relies on the spherical Jeans equation:

$$\frac{1}{\nu} \frac{d}{dr} (\nu \sigma_r^2) + 2 \frac{\beta \sigma_r^2}{r} = - \frac{GM(< r)}{r^2}, \quad (1)$$

where ν is the tracer number density distribution, σ_r is the radial velocity dispersion, β is the velocity anisotropy, $M(< r)$ is the enclosed mass and G is Newton’s gravitational constant. The velocity anisotropy, β , is defined as $\beta = 1 - \frac{\sigma_t^2}{2\sigma_r^2}$, where σ_t is the tangential velocity dispersion. The product $\nu(r)\sigma_r^2(r)$ is typically obtained through deprojection of $\Sigma(R)\sigma_P^2(R)$, where $\sigma_P(R)$ is the line-of-sight velocity dispersion and $\Sigma(R)$ is the tracer number density at the projected distance R , both of which are observable quantities. Further, models are assumed for $\beta(r)$ and $M(< r)$ and the equation is solved for $\sigma(R)$ via sampling methods such as Markov Chain Monte Carlo (MCMC). This analysis assumes a non-rotating spherical system in a steady pseudo-equilibrium state. These assumptions are known to be violated by Local Group dwarfs, which exhibit ellipticity (McConnachie 2012), signs of rotation (Battaglia et al. 2008; del Pino et al. 2017), and are susceptible to tidal effects from their hosts (Read et al. 2006; Peñarrubia et al. 2009; Ural et al. 2015).

As only the line-of-sight motions of the stellar tracers are known, β is poorly constrained, such that Jeans analysis suffers from the M – β degeneracy. This degeneracy results in a wide range of models that satisfy a set of observational constraints, such that cored and cuspy dark matter profiles

may both provide acceptable fits to line-of-sight data (Strigari et al. 2010). The degeneracy may be broken by including the fourth order projected virial theorem, giving rise to two equalities (Merrifield & Kent 1990):

$$\text{VSP1} = \frac{2}{5} \int_0^\infty GM\nu(5 - 2\beta)\sigma_r^2 r dr = \int_0^\infty \Sigma \langle \sigma_P^4 \rangle R dR \quad (2)$$

and

$$\text{VSP2} = \frac{4}{35} \int_0^\infty GM\nu(7 - 6\beta)\sigma_r^2 r^3 dr = \int_0^\infty \Sigma \langle \sigma_P^4 \rangle R^3 dR, \quad (3)$$

where VSP1 and VSP2 are referred to as the virial shape parameters (i.e. VSPs). Here $\langle \sigma_P^4 \rangle$ is the fourth moment of the line-of-sight velocities. The right-hand sides of Equation 2 and Equation 3 contain quantities that can be directly inferred from data and the left-hand sides contain the same parameters as Equation 1. It is thus possible to place two additional constraints on the velocity anisotropy β . In practice, however, the finite quality of data may result in only a partial breaking of the M – β degeneracy.

Read & Steger (2017) introduced the non-parametric Jeans method, GRAVSPHERE (used in Read et al. 2019), which employs the additional constraints from the VSPs in their MCMC analysis. GRAVSPHERE has been shown to successfully recover dark matter density distributions in mock observations of idealized spherical, triaxial and tidally stripped simulated dwarfs from the GAIA CHALLENGE set¹. The cases for which the method works less well, such as aspherical systems, are evident through poor quality fits to the line-of-sight velocity dispersion. The method has been shown to accurately recover densities at ~ 150 pc from the centre – a key region where core formation is expected to reduce dark matter densities, compared to Λ CDM predictions.

In this work we test PYGRAVSPHERE, a PYTHON implementation of the GRAVSPHERE method, on a sample of simulated dwarf galaxies from a cosmological hydrodynamic simulation of Local Group-like environments. The aim of our work is to establish whether Jeans analysis, under the assumption of spherical symmetry, is a suitable method for constraining the mass profiles of dark matter haloes in a fully cosmological setting and how much information is typically gained through the inclusion of VSPs. We compare the performance of the code with standard dynamical mass estimators and explore the range of radii for which the inferred enclosed mass is accurately recovered. We examine in detail the cases where PYGRAVSPHERE fails and identify the reasons for this as well as potential warning signs.

In Section 2, we describe the suite of simulations used, as well as the setup of PYGRAVSPHERE. Our analysis of PYGRAVSPHERE’s performance on each galaxy and the comparison to standard Jeans methods can be found in Section 3. We summarise our findings and conclude in Section 4.

2 SIMULATIONS

2.1 APOSTLE simulations

In this work, we select analogues of classical dSphs from the APOSTLE suite of cosmological simulations. APOSTLE volumes are zoom-in simulations of Milky Way and

¹ <http://astrowiki.ph.surrey.ac.uk/dokuwiki/>

Andromeda analogue pairs, selected from a dark matter-only volume. The pairs have been chosen to satisfy constraints for the Local Group, such as the total mass, separation and relative velocities. The details of halo selection may be found in [Fattahi et al. \(2016\)](#). Each Milky Way or Andromeda analogue hosts a population of dwarf galaxies. The volumes additionally include isolated dwarfs.

APOSTLE was run with the EAGLE model of galaxy formation ([Schaye et al. 2015](#); [Crain et al. 2015](#)), which is based on the smoothed particle hydrodynamics (SPH) N -body code GADGET-3, an improved version of the GADGET-2 code ([Springel 2005](#)). The original APOSTLE suite consists of five high-resolution cosmological volumes, with dark matter mass resolution of $m_{\text{DM}} = 2.5 - 5 \times 10^4 M_{\odot}$. An extra cosmological volume was also run assuming a SIDM² interaction cross-section of $\sigma/m = 10 \text{ cm}^2 \text{g}^{-1}$. We note that this is an extreme value of the cross-section, which was chosen to explore the formation of largest cores in SIDM. The SIDM implementation within EAGLE was introduced in [Robertson et al. \(2018\)](#), based on the SIDM simulation method described in [Robertson et al. \(2017\)](#).

Each stellar particle in APOSTLE represents a stellar population assumed to follow a [Chabrier \(2003\)](#) initial mass function. Gas particles have initial masses in the range $5 - 10 \times 10^3 M_{\odot}$. APOSTLE resolves Sculptor-mass dwarf galaxies with $\sim 10^2$ - 10^3 stellar particles and Fornax-mass dwarf galaxies with $\sim 10^3$ - 10^4 particles. Further details of the simulations may be found in [Sawala et al. \(2016\)](#), [Fattahi et al. \(2016\)](#) and [Campbell et al. \(2017\)](#).

2.2 Numerical considerations

In order to establish whether GRAVSPHERE reproduces the mass profiles of the simulated dwarfs, we must first define what the “true” mass profile is within the simulations.

The mass profiles of dark matter haloes identified in pure N -body simulations are affected by collisional relaxation. The enclosed mass profiles of haloes are suppressed (relative to a higher resolution simulation) below a radius where the 2-body relaxation time, t_{relax} , is comparable to the age of the Universe, t_0 (see e.g. [Power et al. 2003](#); [Ludlow et al. 2019c](#)). For the typical number of dark matter particles in systems that are considered in this work, the [Power et al. \(2003\)](#) radius, where $t_{\text{relax}} \sim 0.6t_0$, corresponds to ~ 60 per cent of the half-light radius (about 600 pc). Moreover, APOSTLE simulations model dark matter and stars using particles of unequal mass, making them subject to energy equipartition, which artificially inflates galaxy sizes ([Ludlow et al. 2019a,b](#)). These effects are most problematic for systems with stellar half-mass radii smaller than ~ 0.055 of the mean inter-particle separation, corresponding to $\sim 400 - 600$ pc for the APOSTLE simulations. We note, however, that the relaxation times at these radii are still considerably longer than the dynamical times of the stars. Therefore, our simulated dwarfs may be considered to be in an instantaneous steady state. The ability of GRAVSPHERE to recover masses in the innermost regions is of interest in

this work, therefore we will present results below the convergence radius derived by [Power et al. \(2003\)](#) and [Ludlow et al. \(2019c\)](#), although we will interpret these with caution.

The use of the gravitational softening in N -body simulations sets a limit on the central density, such that the innermost regions of simulated haloes exhibit a small artificial core on the scale of the gravitational softening. In comparing GRAVSPHERE to N -body simulations, we thus restrict ourselves to radii greater than 2.8ϵ , where $\epsilon = 134$ pc is the Plummer-equivalent gravitational softening. This is the radius outside which the particle forces become exactly Newtonian.

2.3 Sample of dwarfs

We selected a sample of simulated dwarfs to match the stellar masses of Milky Way classical dwarfs, whilst simultaneously requiring a sufficient over ~ 500 stars). Specifically, the galaxies with similar properties to Fornax were selected. These properties include stellar mass, velocity dispersion and half-light radius. Galaxies satisfying these constraints were further refined to those with no bound gas and those that do not exhibit signs of rotation. We quantify rotation by the fraction of stellar particles which are rotating in the same direction as the total stellar angular momentum vector, f_{corot} . We select galaxies with $f_{\text{corot}} < 0.6$. The sample includes only satellites, defined as the objects within 300 kpc of the Milky Way and Andromeda analogues. Note that, in order to obtain a statistically significant sample, we did not include restrictions on the orbits or star formation histories in the selection of the dwarf analogues.

Properties of the resulting sample of galaxies is plotted in Fig. 1. The stellar masses are computed by summing the total mass of stellar particles identified as bound by the SUBFIND algorithm ([Springel et al. 2001](#); [Dolag et al. 2009](#)). For each dwarf, we calculate the projected half-light radius, R_e , using the following procedure. We project the dwarf along 192 isotropically distributed directions generated with the HEALPIX algorithm ([Górski et al. 2005](#)). To each projection we fit a 3-component 2D Plummer profile (more details may be found in Section 2.4.1) and compute the radius which contains half the projected stellar mass. The mean and standard deviation of these values are represented by the points and their error bars. Similarly, for the velocity dispersion we compute the mass-weighted mean velocity dispersion along each projection. The majority of our sample is similar to Fornax (purple bands in Fig. 1). The velocity dispersion and the half-light radius of Fornax were taken from [McConnachie \(2012\)](#). Stellar masses for Fornax shown in Fig. 1 span the range of values from literature ([McConnachie 2012](#); [de Boer et al. 2012](#)).

The rightmost panel of Fig. 1 shows the sphericity of our sample of dwarfs, defined as the ratio of their minor to major axes, $s = c/a$, computed for the stellar component. The axes have been derived from the eigenvalues of the reduced inertia tensor, computed for the stellar particles (see e.g. [Bett et al. 2007](#)). The purple dashed line is the upper limit set on the sphericity of Fornax, determined by the measured projected ellipticity, $e = 1 - b/a = 0.3$ ([Battaglia et al. 2006](#)). Our sample is typically much less aspherical than Fornax, with an average axis ratio of $c/a \sim 0.9$. This is a consequence of our selection criteria, specifically lack of rotation and the

² The SIDM run has not yet been published. The data has been obtained through a private communication with the APOSTLE team.

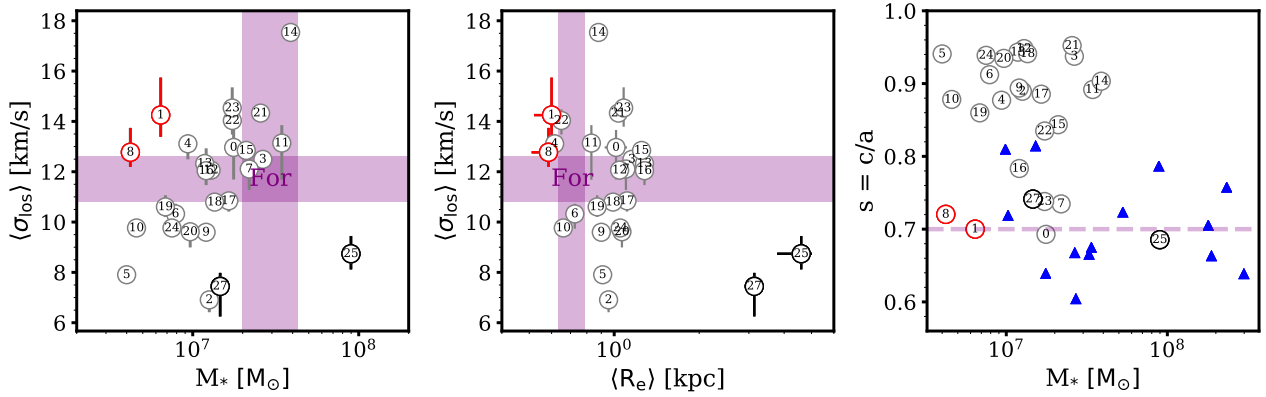


Figure 1. The sample of classical dwarf analogues. SIDM dwarfs are shown with black error bars. Galaxies 25 and 26 are the same SIDM dwarf, viewed from different directions. Galaxies 27 and 28 are also the same SIDM dwarf, viewed from different directions. The selected aspherical dwarf pairs (1 and 29 are the same dwarf, viewed from different directions, and so are 8 and 30) are shown with red error bars. Only one dwarf from each pair is shown (25,27,1,8), as two dwarfs within a pair have the same mean properties. *Left:* mean line-of-sight velocity dispersion as a function of stellar mass. *Middle:* mean line-of-sight velocity dispersion as a function of the mean projected half-light radius. The purple bands show the measurements for Fornax from [McConnachie \(2012\)](#) and [de Boer et al. \(2012\)](#). *Right:* sphericity of our sample of dwarfs compared to the upper limit for Fornax ($c/a \approx 0.7$), which has a 2D ellipticity $e = 0.3$ (purple dashed line). The blue triangles show a sample of 14 isolated APOSTLE dwarfs with sphericity comparable to the upper limit set on Fornax.

lack of gas for the selected sample of dwarfs. These are more likely to be features of dwarf galaxies that have undergone stripping, which tends to reduce asphericity ([Barber et al. 2015](#)). In order to further investigate the effects of sphericity we include a sample of isolated dwarfs with $c/a \sim 0.7$ (blue triangles in Fig. 1). The sample has been chosen to contain galaxies that have less gas than stellar mass and for which gas does not dominate by mass within the 3D half-mass radius of the stars. Since the GRAVSPHERE method explicitly account for the mass contributed by the stars, but not by gas, when comparing GRAVSPHERE’s performance for these dwarfs with the “true” values, we compare to the combined mass in gas and dark matter.

In order to generate the photometric and kinematic data required by GRAVSPHERE, we obtained the stellar positions and velocities for particles in each subhalo, which were classified as bound by SUBFIND ([Dolag et al. 2009](#)). The positions of the stellar particles were centred at their 3D centre of mass, calculated using the “shrinking spheres” algorithm ([Power et al. 2003](#)). The positions and velocities were then projected along one of three different lines of sight – major, minor or intermediate axes of the subhalos. The stellar particles within $2R_{2D}$, where R_{2D} is the projected radius that contains half the stellar particle mass, were randomly sampled, providing 500 - 2500 particles for the kinematic sample. The photometric sample included all stellar particles within $2R_{2D}$. The velocities within the kinematic sample were perturbed with Gaussian noise with a standard deviation of 2 km s^{-1} . The mass within $3R_{2D}$ has additionally been provided, $M(< 3R_{2D})$, so that the mass of the stellar component may be included in the analysis.

Overall, 25 galaxies and their projections were selected randomly from the sample. Two extra galaxies from the APOSTLE SIDM run were also added, each projected along two different directions (Galaxies 25-28). Finally, an extra two galaxies with relatively low sphericity ($c/a \sim 0.7$) were chosen from the existing sample and projected along a dif-

ferent axis (Galaxy 29, which is Galaxy 1 projected along a different direction and Galaxy 30, which is Galaxy 8 projected along a different direction).

2.4 The PYGRAVSPHERE code

In this work we present a PYTHON implementation of the GRAVSPHERE method. PYGRAVSPHERE is an open source software³. As in the work of [Read & Steger \(2017\)](#), PYGRAVSPHERE is based on the affine-invariant ensemble sampler EMCEE ([Foreman-Mackey et al. 2013](#)). EMCEE differs from the classic Metropolis-Hasting algorithm in that each individual Markov chain, or “walker”, communicates with the other “walkers” at each step, thus allowing the chains to converge on high-likelihood regions of the parameter space faster. EMCEE has parallel functionality, which we exploit in this work. In the following, we outline the assumptions and parameters that enter into our EMCEE setup.

2.4.1 EMCEE parameters

As in [Read & Steger \(2017\)](#), to parametrize the dark matter distribution, PYGRAVSPHERE employs a split power-law model with 5 spatial bins defined as spaced fractions of the half-light radius⁴, R_e , with bins $r_j = [0.25, 0.5, 1, 2, 4] R_e$.

³ <https://github.com/AnnaGenina/pyGravSphere>

⁴ In this work we use multiple definitions of the half-mass radius, which we list here for the purposes of clarification. R_{2D} is the projected radius which contains half of a dwarf’s stellar mass and it is computed by direct summation. R_e is the projected radius containing half the stellar mass, derived from a 3-component Plummer profile fit to the *sample* of stellar particle data. We frequently refer to R_e as the half-light radius.

Within each bin, the density follows a power law defined by slopes γ_j . The overall distribution is described by

$$\rho_{\text{dm}}(r) = \begin{cases} \rho_0 \left(\frac{r}{r_0}\right)^{-\gamma_0}, & r < r_0 \\ \rho_0 \left(\frac{r}{r_{j+1}}\right)^{-\gamma_{j+1}} \prod_{n=0}^{n<j+1} \left(\frac{r_{n+1}}{r_n}\right)^{-\gamma_{n+1}}, & r_j < r < r_{j+1} \end{cases} \quad (4)$$

where ρ_0 is the density at r_0 . Beyond the outermost bin, the power law is extrapolated. Note that this radial extent typically covers the positions of available kinematic tracers.

For the light profile, PYGRAVSPHERE uses a sum of three Plummer (1911) components ($N_P = 3$):

$$v(r) = \sum_j^{N_P} \frac{3M_j}{4\pi a_j^3} \left(1 + \frac{r^2}{a_j^2}\right)^{-5/2}, \quad (5)$$

where M_j and a_j are the relative weight and spatial extent of each component, respectively. This distribution is straightforward to project, yielding:

$$\Sigma(R) = \sum_j^{N_P} \frac{M_j}{\pi a_j^2} \left(1 + \frac{R^2}{a_j^2}\right)^{-2}. \quad (6)$$

The velocity anisotropy is parametrized following Baes & van Hese (2007):

$$\beta(r) = \beta_0 + (\beta_\infty - \beta_0) \frac{1}{1 + \left(\frac{r_0}{r}\right)^\eta}, \quad (7)$$

where β_0 is the central value of the anisotropy, β_∞ is the value at infinity, r_0 is the radius of transition and η is its steepness.

2.4.2 PYGRAVSPHERE data input

The photometric sample of stars is split into bins of 15 particles. We weight each particle by the relative number of stars it represents (i.e. we define the weight of each particle as $w_p = m_p N_{\text{tot}} / M(< 3R_{2D})$, where N_{tot} is the total number of particles in the sample). For each photometric bin we calculate the Poisson errors and use the LMFIT algorithm to obtain the best 3-component Plummer fit, which is then input into EMCÉE, following Equation 6.

The kinematic data are also split into bins of 15 particles. The error in each bin is computed by adding the Poisson and sampling errors in quadrature, where we again weight each particle by w_p . This procedure is described in detail in Read & Steger (2017). The effect of the number of particles per bin was explored in Read & Steger (2017), who found little impact on their results.

We use the same kinematic bins to compute the mean and errors of the two VSPs. The fourth moment of the velocity distribution is computed for each bin. Because VSP2 is sensitive to the behaviour of the velocity dispersion profile in the outer regions (due to the R^3 term), we fit a power law to the computed fourth moment velocity profile outside of the projected half-light radius and extrapolate the power law as in Read et al. (2018).

Table 1. Default GRAVSPHERE priors

Property	Parameter	Prior
Dark Matter	$\log_{10} \rho_0$	[5, 10]
	$\gamma_{0,1,2,3,4}$	[0, 3], $\Delta\gamma_{\text{max}} = 1$
Anisotropy	$\tilde{\beta}_0$	[-1, 1]
	$\tilde{\beta}_\infty$	[-1, 1]
	$\log_{10} r_0$	$\log_{10}[R_e/2, 2R_e]$
	η	[1, 3]
Tracers	$\log_{10} M_j$	$\log_{10}[M_{\text{bf},j}/2, 3/2M_{\text{bf},j}]$
	a_j	$[a_{\text{bf},j}/2, 3/2a_{\text{bf},j}]$
Baryons	$\log_{10} M_*$	$\log_{10}[0.75M(< 3R_{2D}), 1.25M(< 3R_{2D})]$

2.4.3 EMCÉE set-up and priors

The priors on each of the parameters in the default PYGRAVSPHERE set-up are shown in Table 1. Parameters $\log_{10} M_j$ and a_j of the best 3-component Plummer fit are allowed to vary within 50 per cent of their linear best-fit values, as determined by LMFIT, while the stellar masses $\log_{10} M_*$ were varied within 25 per cent of the $M(< 3R_{2D})$ value.

Whilst the starting positions of walkers are ideally generated to follow a uniform distribution, this is difficult to achieve when the values of the dark matter slope, γ , in each radial bin, r_j , are constrained to monotonically increase. We find that typically ~ 5 per cent of the initially generated walker positions fall within these defined bounds. If the chains are allowed to run for long enough, the walkers that are “stuck” in forbidden regions of the parameter space may eventually make their way to the allowed regions. This process is, however, dependent on the efficiency of the active walkers in probing the posterior likelihood function. In cases where the likelihood is multimodal, for example, some regions of the hyperspace will not be probed due to the nature of the ensemble sampler, where the walkers communicate with each other, unlike in the classical Metropolis-Hastings algorithm.

We thus use the following procedure to generate the initial walker positions. For each walker, we generate the free parameters following a uniform distribution. We then throw away the walkers that do not satisfy our γ prior constraints. For the discarded walker positions we generate new ones, accepting those that satisfy the constraints and rejecting the others. This procedure is repeated recursively until each walker has a randomly generated initial position that satisfies the constraints. The effective priors resulting from this procedure and the advantages of the method over the one implemented in the original works using GRAVSPHERE (e.g. Read & Steger 2017; Read et al. 2018) are discussed in Appendix A.

We use 1000 walkers to probe the posterior distribution. The walkers are run for 10^4 steps as a “burn-in” measure, and then for a further 10^4 steps. The results presented in Appendix A suggest that our walkers are converged after $\sim 6 \times 10^3$ steps, so the above choices are rather extreme.

Since the anisotropy parameter, β , can take on values between 1 and $-\infty$, one would benefit from transforming this

into a finite range. As in [Read & Steger \(2017\)](#), we use the symmetrized anisotropy parameter,

$$\tilde{\beta} = \frac{\beta}{2 - \beta}, \quad \text{with} \quad -1 < \tilde{\beta} < 1. \quad (8)$$

This allows the MCMC to probe the entire range of the allowed anisotropy values. In practice, we apply the constraints $\tilde{\beta}_0 > -0.95$ and $\tilde{\beta}_\infty > -0.95$, as for more negative values the calculation becomes numerically unstable.

PYGRAVSPHERE solves the Jeans equation for the projected velocity dispersion profile, $\sigma_P(R)$. It additionally fits the projected number density distribution, $\Sigma(R)$, and the two VSPs. The likelihood is calculated by adding the chi-squared of these four components:

$$\ln \mathcal{L} = -\frac{1}{2} \left(\chi_{\sigma_{LOS}}^2 + \chi_{\Sigma}^2 + \chi_{VSP1}^2 + \chi_{VSP2}^2 \right). \quad (9)$$

3 RESULTS

In this section we present the performance of the GRAVSPHERE method, under a default setup, on each of the dwarfs in our sample. We further quantify its global performance, for the entire sample, and compare to more standard Jeans analysis approaches. We identify the causes of bias and scatter in the recovered enclosed mass profiles.

3.1 Individual dwarfs

[Fig. 2](#) shows the recovery by GRAVSPHERE of the cumulative mass profile and the velocity anisotropy profile for each dwarf in our sample. The “true” mass and anisotropy profiles are displayed in blue and the GRAVSPHERE results in grey shaded bands. To generate the GRAVSPHERE profiles we took 10^5 random samples from the output MCMC chains and for each radial position computed the median and the 68th and 95th confidence levels. The choice of 10^5 samples is sufficient to produce representative posteriors, but is otherwise arbitrary.

Simulated dwarf mass profiles were computed by summing dark matter particle masses one-by-one radially from the centre of the dwarf, where we defined the centre as the centre of mass of the stellar component. In order to compute the stellar velocity anisotropy in the simulated dwarfs we bin the stars into 50 logarithmically spaced bins, starting from the position of the star that is closest to the centre of mass and ending at the outermost star. We then reduce the number of bins and widen the bin edges such that each bin has at least 50 stars within. We construct 1σ error bars by taking 1000 random samples of 25 stars with replacement and computing the standard deviation in the velocity anisotropy of each bin.

In this analysis we focus on the key region within the half-light radius of each galaxy (solid vertical blue line). It is clear that, for individual systems, GRAVSPHERE gives generally unbiased results. The simulated dwarf mass profiles are typically contained within the 68 per cent confidence limits set by PYGRAVSPHERE, although the uncertainties can be large. Even for the SIDM dwarfs (Galaxies 26,27,28 in

particular), where the enclosed mass is systematically overestimated in central regions, the true profiles are still contained within the 95 per cent confidence regions. These objects have large cores, comparable to their half-light radii (~ 3 kpc), with a steep drop in the outer density, steeper than the $\gamma = 3$ limit allowed by the default GRAVSPHERE priors. There are, however, notable exceptions. For instance, the enclosed masses for Galaxy 3 and Galaxy 18 are significantly underestimated, which may lead to an incorrect inference of a cored profile, when in reality there is a cusp. For Galaxy 18, the mismatch between the inferred and simulated velocity anisotropy profile is particularly evident. We will return to this issue in [Section 3.4.2](#).

3.2 Comparing to standard estimators

In this section, we compare the performance of GRAVSPHERE in recovering enclosed masses to three mass estimators in the literature. The estimator provided by [Wolf et al. \(2010\)](#) gives the mass enclosed within the deprojected half-light radius R_3 , with $R_3 \sim 4/3R_e$; the [Walker et al. \(2009\)](#) estimator at the the projected half-light radius, R_e . Another estimator has been derived by [Campbell et al. \(2017\)](#) for the mass within $1.44R_{2D}$, where R_{2D} is the projected radius containing half the stellar mass. The latter has been calibrated on dwarfs from the APOSTLE suite of simulations that we use here. We exclude the estimator derived by [Errani et al. \(2018\)](#), which we find produces similar results to those of [Campbell et al. \(2017\)](#).

We calculate the half-light radius, as before, by fitting a 3-component Plummer profile to the surface brightness data for each dwarf and finding the radius that encloses half of the stellar mass. We calculate the mean velocity dispersion and the associated errors using the technique of [Walker et al. \(2006\)](#), where we incorporate weighting by the number of stars per stellar particle, w_p , in the likelihood function.

In the top panel of [Fig. 3](#), we show the median accuracy of the enclosed mass computed with PYGRAVSPHERE for the sample of dwarfs, and the 68 per cent confidence levels, as a function of normalised radius, R/R_e . We use the following procedure to compute the global radial accuracy and the associated confidence levels. For each galaxy and for each distance, R , we obtain a cumulative mass distribution from 10^5 random samples of the MCMC posteriors. We then use this cumulative distribution for Monte Carlo sampling of accuracies, combining the samples from all galaxies at each distance. This allows us to take into account the asymmetry in the GRAVSPHERE confidence levels, as may be seen in [Fig. 2](#).

The lower axis limit on R/R_e in [Fig. 3](#) has been chosen to be the average value of $2.8\epsilon/R_e$ for our sample and the upper axis limits so as to contain the smallest dark matter halo in the sample. For the smaller values of R/R_e , we only compute the accuracies and associated errors for galaxies where this fraction is above 2.8ϵ . Below $2.8\epsilon/R_e$ the scatter increases significantly, but this is due to particle noise.

In purple, we show the sample without the 4 SIDM galaxies and in black the entire sample of 31 simulated dwarfs. The symbols with error bars show the performance of the alternative mass estimators. Each estimator is used with two definitions of the half-light radius: one derived from the best-fit 3-component Plummer profile (circles), and one

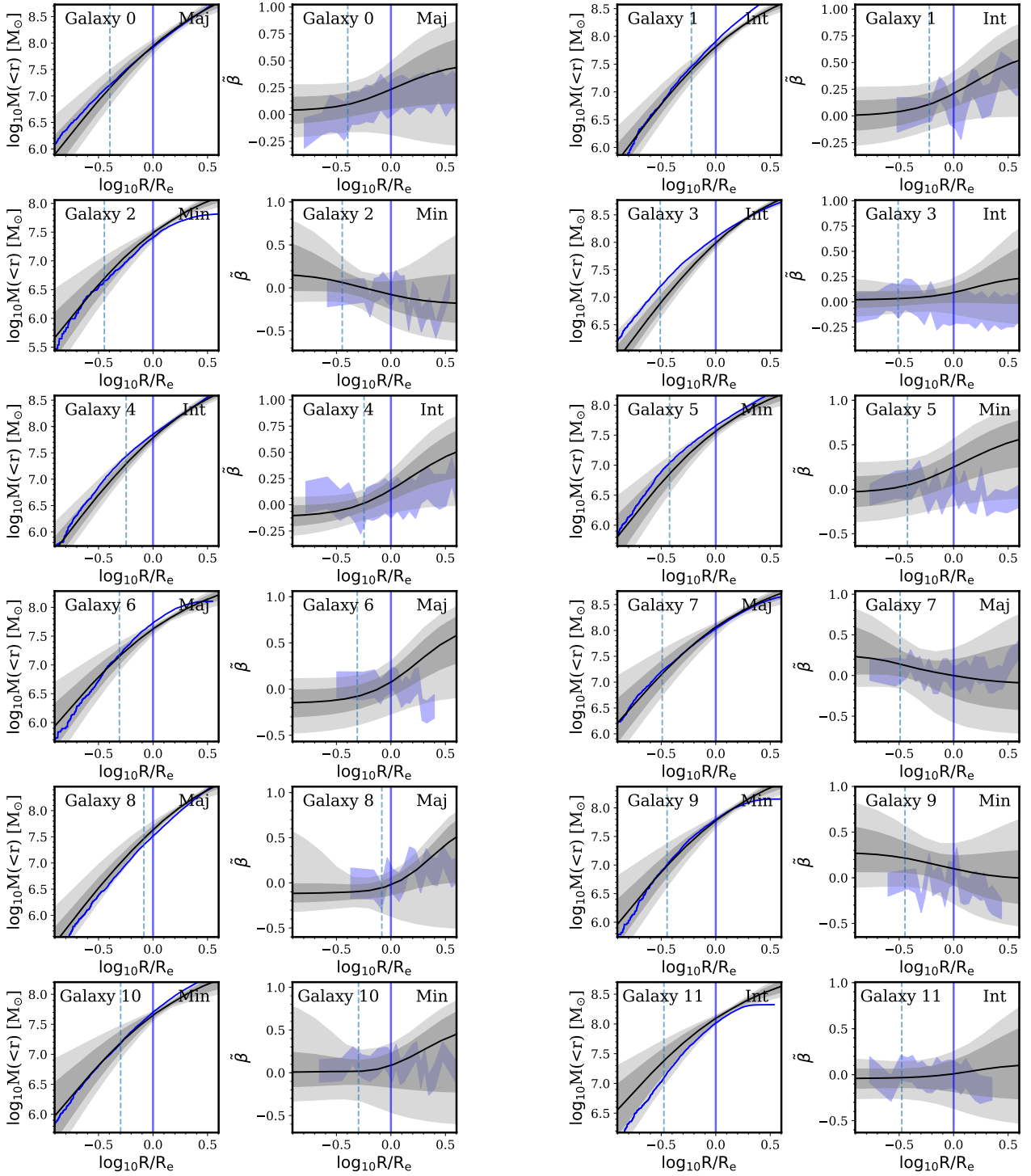
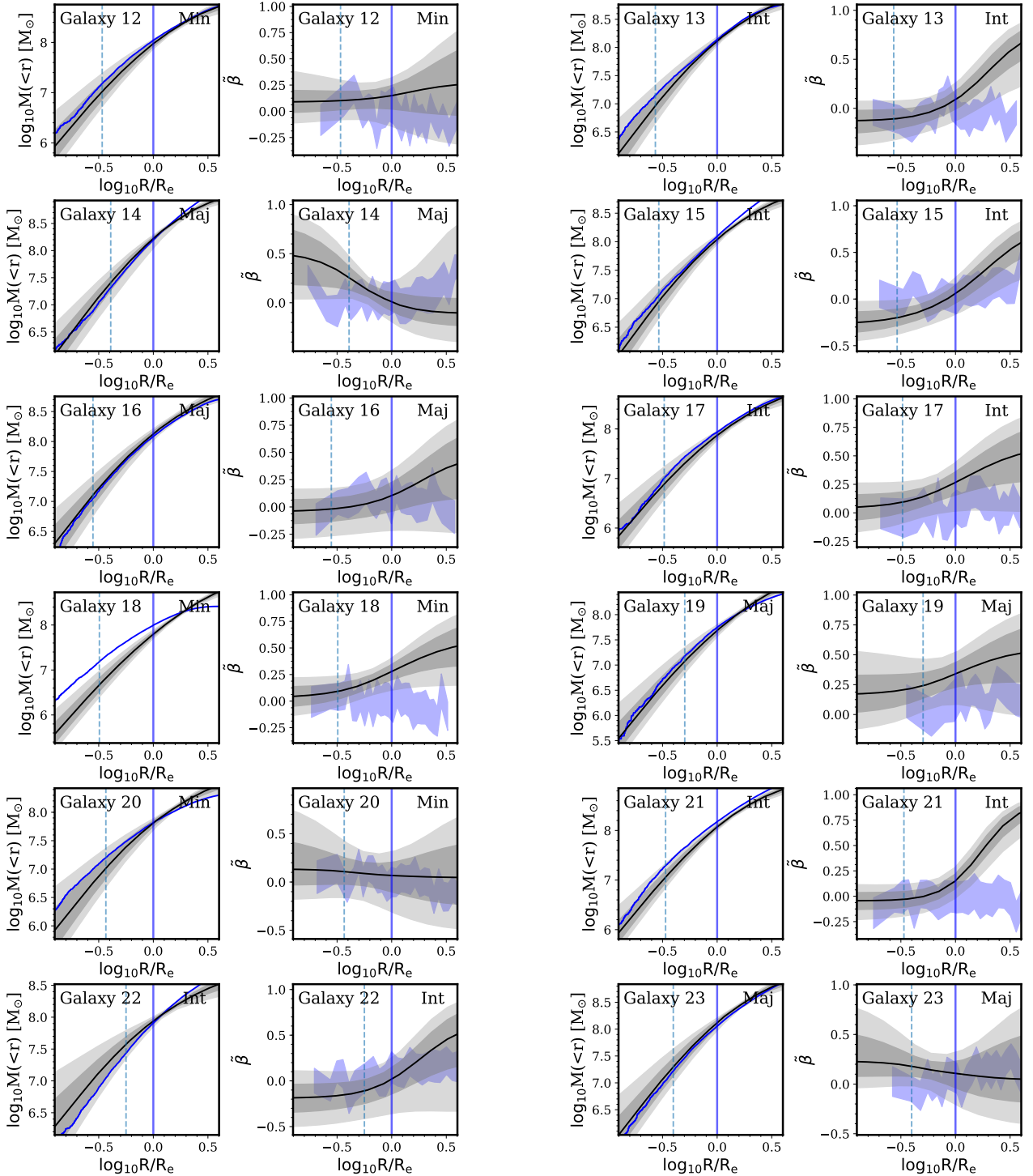


Figure 2. Enclosed dynamical mass profiles and symmetrized anisotropy, β , profiles as recovered by GRAVSPHERE. The black lines and the grey shaded bands display the median, 68 and 95 per cent confidence limits. The “true” mass profiles measured directly from the simulation are shown in blue. The solid vertical blue line shows the location of the projected half-light radius and the dashed blue line shows $2.8\epsilon \sim 0.380$ pc, which is close to the convergence radius for these systems. The “true” velocity anisotropy, as measured directly from the stellar particles, is shown with a shaded blue band. The top left corners identify each galaxy and the top right corners show the axis along which the galaxy is viewed.

Figure 2 – *continued*

using the projected radius at which half of the mass in the photometric sample is contained (squares). These radii can, in fact, be quite different. We find that R_{2D} is always below R_e and takes a mean value $\langle R_{2D} \rangle \sim 0.76R_e$. Estimator accuracies determined by using R_{2D} are shown at this mean value for the whole sample. Interestingly, the use of R_e provides significantly more accurate results. This is consistent with the findings of [González-Samaniego et al. \(2017\)](#). This

result does not change if we obtain R_{2D} from all bound stars, where $\langle R_{2D, \text{all}} \rangle \sim 1.22R_e$.

From the top panel of Fig. 3 it is clear that at the half-light radius GRAVSPHERE performs just as well as the [Wolf et al. \(2010\)](#) and [Walker et al. \(2009\)](#) estimators, and with similar scatter. The scatter is smaller for the CDM sample. The inferred masses are, on average, very accurate across the entire radial range, with the scatter becoming more signif-

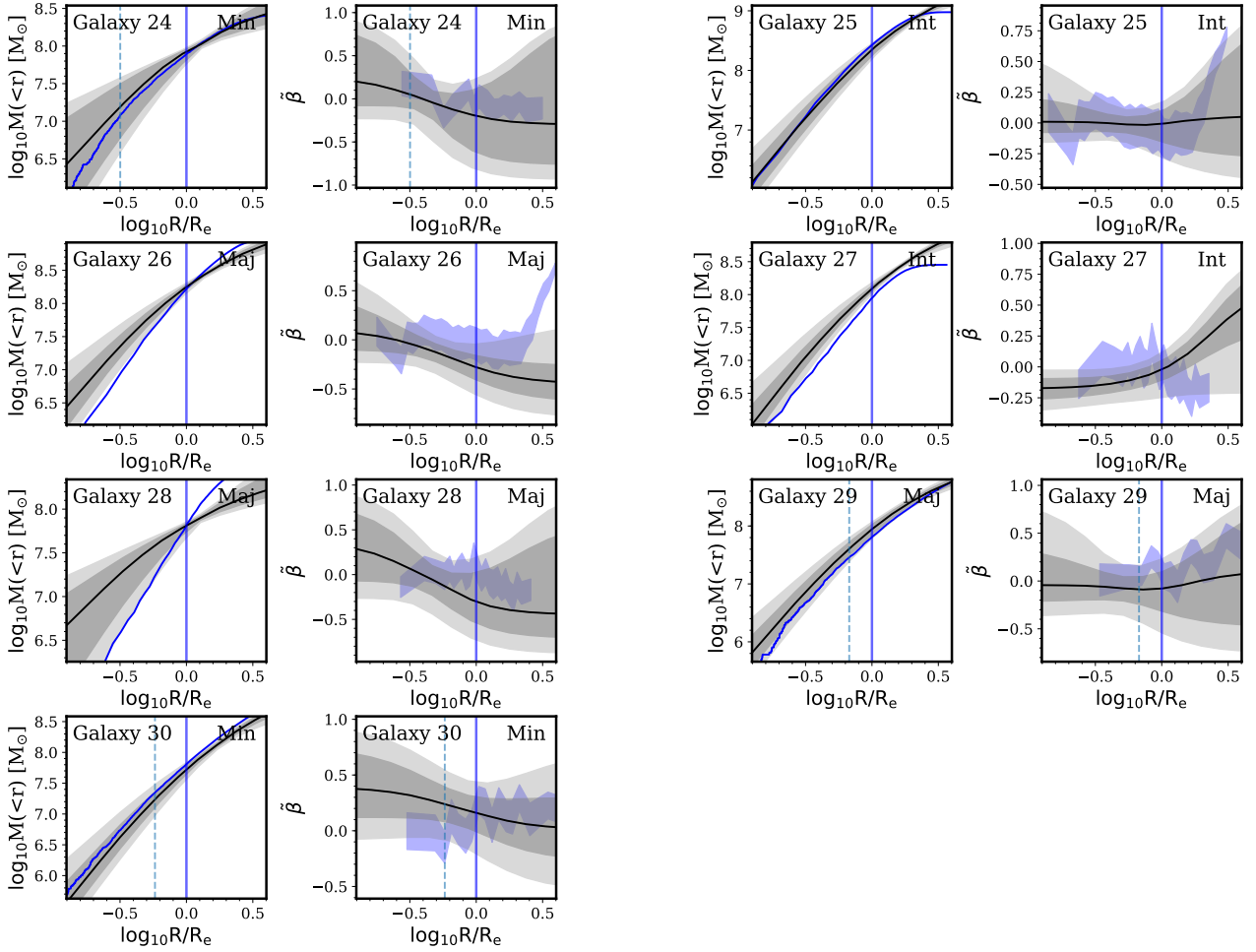


Figure 2 – *continued* Galaxies 25 through 28 are from SIDM simulations.

icant in the innermost regions as well as the outer regions. For the large values of R/R_e this is caused by the lack of kinematic tracers. Moreover, our priors permit only a narrow range of slopes ($0 < \gamma < 3$), whilst our sample is expected to have undergone tidal effects, resulting in an outer slope $\gamma \sim 4$ (Peñarrubia et al. 2009). Nevertheless, the estimate is accurate, on average, out to $\sim 3R_e$, with a root mean square value⁵ (RMS) of only 0.06. It is clear that the masses for SIDM dwarfs are significantly overestimated in the inner regions, resulting in an increased scatter for the entire sample. We will return to this issue in Section 3.4.1.

In the bottom panel of Fig. 3 we show the recovery by PYGRAVSPHERE of the dark matter density profiles of our sample of dwarfs. Remarkably, the density recovery is also accurate across the entire radial range (RMS = 0.06) and the scatter is very similar for the samples including and excluding SIDM dwarfs. In the innermost regions, the scatter

⁵ We define $\text{RMS} = \sqrt{\frac{1}{N} \sum_{i=1}^N (M_{\text{calc}}/M_{\text{true}} - 1)^2}$, where M_{calc} is the mass obtained through PYGRAVSPHERE, or another method, N is the number of radial intervals at which M_{calc} is computed and M_{true} is the true enclosed mass at these intervals, found directly from the simulation. We use ~ 30 radial intervals to construct Fig. 3.

is only ~ 30 per cent. In fig.5 of Read et al. (2019) it can be seen that, for a dwarf of Fornax-like pre-infall halo mass, the core and cusp-like densities, ρ_{150} , differ by a factor of at least ~ 3.5 . The spatial resolution of our simulations does not allow us to probe radii below ~ 380 pc; however, if GRAVSPHERE provides similar accuracy and scatter for ρ_{150} (corresponding to $\log_{10} R/R_e \sim -0.7$ for a Fornax-size dwarf), it is certainly possible to differentiate between the core and cusp-like densities, provided complete core formation below the half-light radius and no reduction of central dark matter density due to tides (Read et al. 2016).

3.3 Comparison to Jeans analysis without VSPs

We now compare the performance of GRAVSPHERE to that of more conventional Jeans approaches.

3.3.1 Excluding the VSPs: Broken Power Law

What is gained by including the virial shape parameters? We repeat our GRAVSPHERE run, this time excluding the two VSPs from Equation 9. The results are shown in the top left of Fig. 4. It can be seen that the accuracy in the outer regions has suffered from excluding the VSPs. The

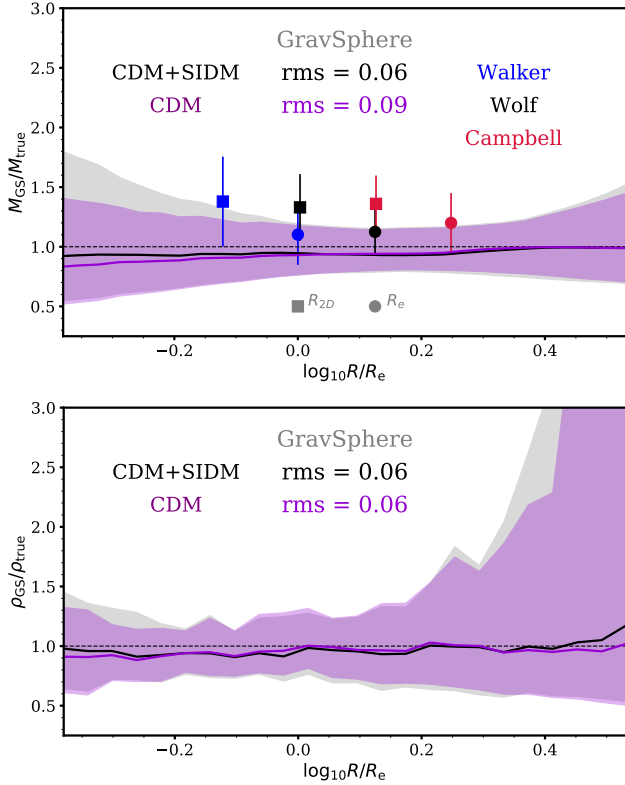


Figure 3. *Top:* ratio of the recovered to true mass as a function of the fraction of half-light radius, R_e . The black line and grey shaded bands show the median and 68 per cent confidence limits for the entire galaxy sample. The purple line and the corresponding shaded bands show the sample of Λ CDM dwarfs only (excluding SIDM dwarfs). The symbols and their error bars show the accuracy of standard estimators, as identified by their colours. The circles are for the half-light radii derived from the 3-component Plummer profile fit, R_e . The squares are for the radii enclosing half the stellar mass in projection, R_{2D} . *Bottom:* ratio of the recovered to true density as a function of the fraction of half-light radius, R_e .

bottom panel shows the ratio of the upper and lower errors (84th and 16th percentiles) compared to the default GRAVSPHERE run (including the VSPs). It is evident that the scatter has increased beyond the half-light radius. This suggests that GRAVSPHERE runs that exclude the VSPs result in a wider range of allowed models. Evidently, the inclusion of VSPs plays a key role in minimizing the scatter in allowed anisotropy models, particularly in the outer regions.

3.3.2 Comparison to Zhao (1996) profile

We next compare the performance of GRAVSPHERE to the method outlined by Bonnavard et al. (2015a), who used the profile proposed by Zhao (1996) to parametrize the dark matter distribution:

$$\rho_{\text{dm}} = \frac{\rho_0}{\left(\frac{r}{r_s}\right)^{-\gamma} \left(1 + \left(\frac{r}{r_s}\right)^\alpha\right)^{\frac{\beta-\gamma}{\alpha}}} \quad (10)$$

Table 2. Zhao (1996)+ γ, r_s MCMC priors and the cuts applied in post-processing

Parameter	Prior	Constraint
$\log_{10} \rho_s$	[5, 13]	
$\log_{10} r_s$	[-3, 1]	$\log_{10} r_s \geq \log_{10} R_e$
α	[0.5, 3]	
β	[3, 7]	
γ	[0, 1.5]	$\gamma \leq 1$

where r_s and ρ_0 are the scale radius and scale density, γ is the inner slope, β the outer slope and α governs the steepness of transition between γ and β .

The priors for this run, which we refer to as Zhao + γ, r_s , are given in Table 2. The method requires two post-processing cuts: one on $\gamma \leq 1$, which was shown to reduce the overall scatter, and another on $r_s \geq R_e$, which weeds out unphysical models from the fit. The results are shown in the bottom-left of Fig. 4.

Clearly this method underestimates enclosed masses. We propose that this loss of accuracy is due to a much wider range of outer slopes, β , allowed by the Zhao + γ, r_s model, which causes a redistribution of mass in the proposed mass models. To test this, we repeat our GRAVSPHERE run, this time allowing the slopes $\gamma_{1,2,3,4}$ to vary between 0 and 10. We additionally remove the constraint on the maximum difference between successive slopes γ_j , but do require them to increase outwards. The results are shown in the bottom-right panel of Fig. 4, where we have recovered this decrease in accuracy in the inner regions. There is also more mass within the deprojected half-light radius of the dwarfs. This is likely a consequence of the broken power law slopes, γ_j , being independent of each other in the absence of any constraint on the profile smoothness, $\Delta\gamma_{\text{max}}$, thus allowing GRAVSPHERE to modify the density profile as needed to best fit the data.

3.3.3 Constant anisotropy and no VSPs

We now explore the performance of GRAVSPHERE under the assumption of constant anisotropy and no VSPs. From Fig. 2, it is clear that the vast majority of our simulated dwarfs have nearly constant stellar velocity anisotropy profiles. It is therefore possible that forcing the anisotropy profile to be constant with distance may force the MCMC algorithm to select better models. The comparison with GRAVSPHERE is shown in the top right of Fig. 4. Similar accuracy to GRAVSPHERE is achieved across the entire radial range. The errors have decreased in the innermost regions, but outside R_e the errors are significantly larger, reflecting the lack of flexibility as compared to the Baes & van Hese (2007) profile.

Based on the sample of dwarfs presented in this paper, our simulations suggest that dwarfs may have anisotropy profiles that are well described by a constant value of β . For this sample, the assumption of constant velocity anisotropy is sufficient to accurately recover mass profiles in the innermost regions of dwarfs and this does not require the use of the VSPs.

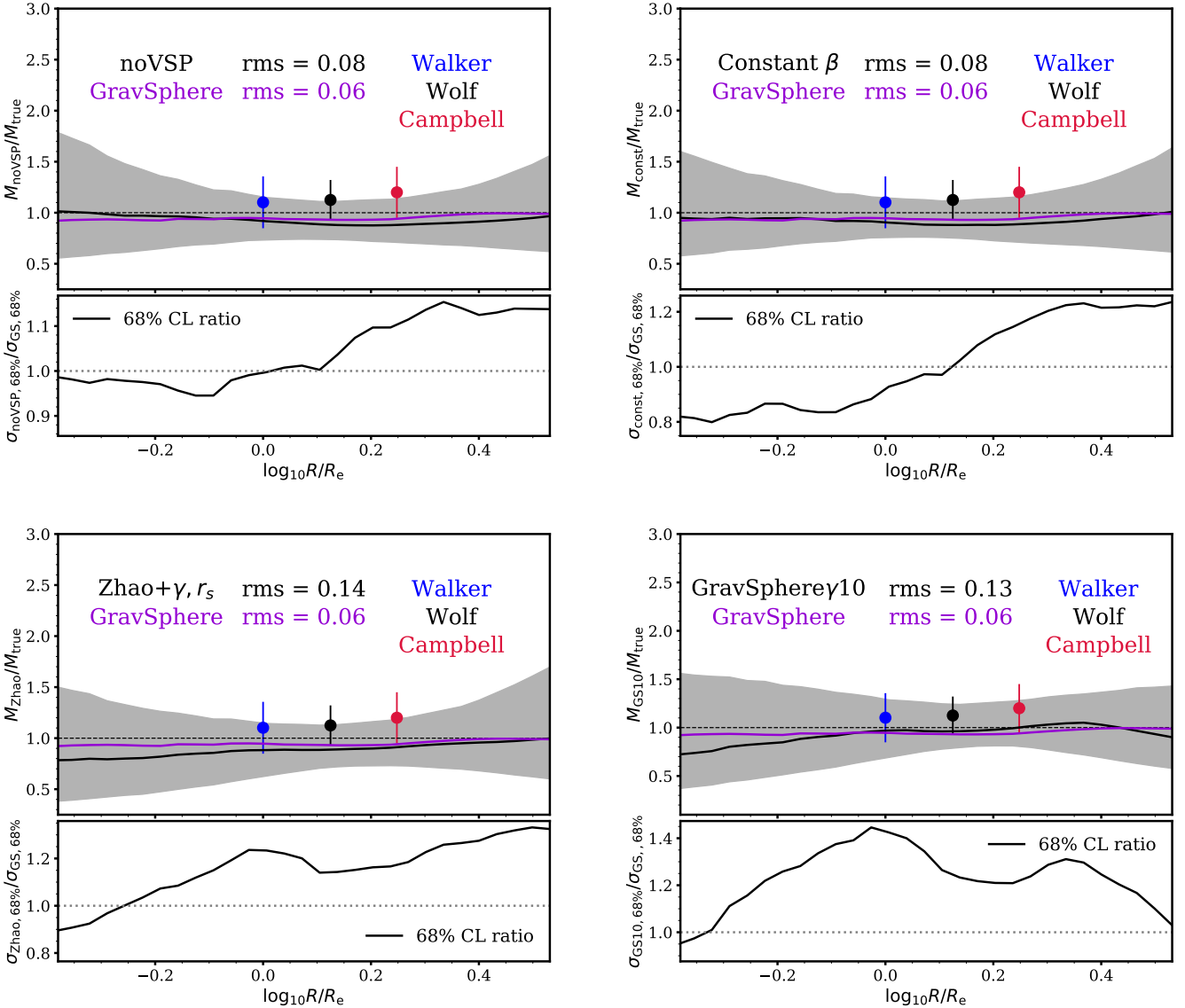


Figure 4. *Top left:* accuracy achieved with GRAVSPHERE assumptions, but excluding the VSPs (black line and grey bands). The purple line shows the median of the default run (including VSPs). The bottom subplot shows the magnitude ratio of the 68 per cent confidence intervals between the “noVSP” and default GRAVSPHERE results. *Top right:* accuracy obtained assuming constant anisotropy and no VSPs. *Bottom left:* accuracy achieved assuming a Zhao (1996) profile and using priors as outlined in Table 2, together with post-processing cuts ($\gamma < 1$ and $r_s > R_e$). *Bottom right:* The accuracy obtained with priors $\gamma_{0,1} = [0, 3]$, $\gamma_{2,3,4} = [0, 10]$ and $\Delta\gamma_{\text{max}} = 10$. The symbols are as in Fig. 3.

3.4 When does GRAVSPHERE fail?

We now explore possible origins of scatter in the top panel of Fig. 3. Projection effects and asphericity are of particular interest (Genina et al. 2018). We have also seen that in some cases (e.g. Galaxy 18) the recovered enclosed mass is underestimated due to GRAVSPHERE preferring more radially biased velocity anisotropy profiles than those measured. In this section we investigate why this occurs.

3.4.1 Line-of-sight effects

Our sample has been chosen to contain galaxies projected along their principal axes. We can therefore split our sam-

ple into 3 categories: dwarfs seen along the minor, major and intermediate axes, and examine the accuracy of GRAVSPHERE in recovering mass profiles in each case. The results are shown in the top panel of Fig. 5. The two pairs of dwarfs (1, 29 and 8, 30) that have minor-to-major axis ratios of ~ 0.7 are shown individually.

For systems viewed along the minor or intermediate axis, GRAVSPHERE recovers enclosed masses with similar accuracy (RMS= 0.13–0.14), and a systematic underestimate. For dwarfs viewed along the major axis, PYGRAVSPHERE returns accurate enclosed masses; however, near the centre, the masses are overestimated by up to 25 per cent. This is entirely due to the two SIDM dwarfs viewed along the ma-

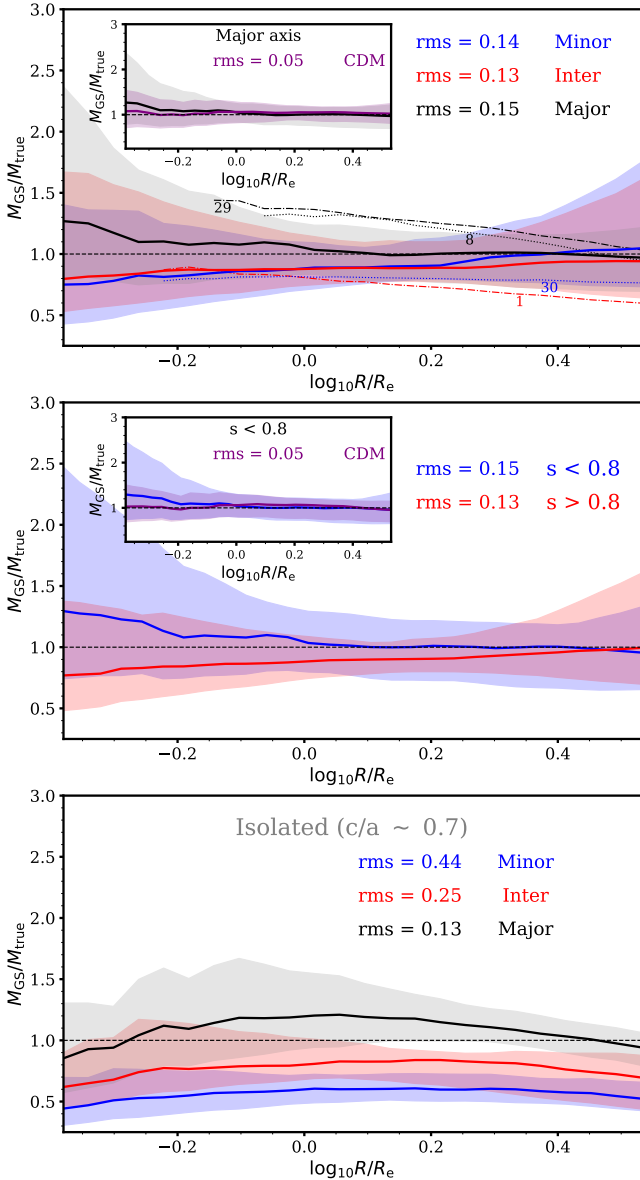


Figure 5. *Top:* line-of-sight effects on the accuracy of the mass profile recovery with GRAVSPHERE. The sample of galaxies is split into those viewed along the minor (blue line and bands), intermediate (red) and major (black) axis. The pairs of dwarfs 1, 29 and 8, 30 are plotted individually, as labelled. The inset shows a comparison, for the major axis, with the CDM-only sample. *Middle:* accuracy for two sets of dwarfs: those that are more spherical (red, $s > 0.8$) and those that are less spherical (blue, $s < 0.8$). The inset shows a comparison, for aspherical dwarfs, with the CDM-only sample. *Bottom:* accuracy of mass profile recovery for fourteen isolated dwarfs, with spheriticities ~ 0.7 , viewed along their three principal axes.

major axis (see the inset in the top panel of Fig. 5, showing CDM dwarfs only). Without the SIDM dwarfs, the major axis RMS is ~ 0.05 . This distinction is due to their enhanced asphericity, as we explain below.

In the middle of Fig. 5 our sample of dwarfs is split into those which have a minor-to-major axis ratio $s > 0.8$ (red) and those with $s < 0.8$ (blue). The aspherical dwarfs resemble the sample viewed along the major axis. In fact,

the majority of dwarfs within our sample with $s < 0.8$ have been projected along the major axis. If we exclude the SIDM dwarfs 26 and 29 (see inset figure), the mass profile recovery is in fact accurate (RMS=0.05), with minimal scatter. It is thus the asphericity of SIDM dwarfs coupled to their major axis projection which results in GRAVSPHERE’s poor performance for these galaxies.

We now investigate the line-of-sight effects for a sample of aspherical dwarfs. We select a sample of isolated dwarfs with masses and sphericities comparable to Fornax. The sphericities of this sample of 14 dwarfs can be seen on the right panel of Fig. 1. These dwarfs have been chosen to contain less mass in gas than in stars and have no neighbour galaxies within a radius of 100 kpc. We have explicitly checked that the gas mass does not exceed the stellar mass within the half-light radius of these dwarfs and that they show no signs of rotation, as quantified by the fraction of stars co-rotating with the net stellar angular momentum.

The results are shown in the bottom panel of Fig. 5, where the pattern with the line-of-sight seen in the top panel of Fig. 5 is repeated. Note the reducing accuracy for the outer regions of these dwarfs. This is caused by gas dominating over stars outside the half-light radius. For this reason, when assessing the accuracy, we compare the GRAVSPHERE result with the cumulative mass of both gas and dark matter.

If Fornax has a sphericity of 0.7 (Battaglia et al. 2006), similar to our isolated dwarf sample, and is viewed along the intermediate axis direction, with an on-the-sky ellipticity of 0.3, our results suggest that GRAVSPHERE will underestimate its mass profile across the entire radial range by ~ 25 per cent. This assumes that Fornax has not been significantly tidally stripped and is thus similar to dwarfs in this isolated sample. Fornax is known to have a particularly low orbital eccentricity, $\langle e \rangle \sim 0.35$ (Fritz et al. 2018), and its relatively recent star formation would suggest a late infall time (Read et al. 2019).

We note that our sample consists entirely of dwarfs projected along the three principal axes, which may not be representative of inclinations and alignments of Local Group dwarfs. It is, however, clear that one must be cautious of systems appearing particularly spherical on the sky, as these may correspond to major axis projections of prolate systems, leading to an overestimation of the enclosed mass (González-Samaniego et al. 2017). In the bottom panel of Fig. 5 it can be seen that this overestimation, though noisy in the centre, appears to be highest near the half-light radius, which may lead to an incorrect inference of a dark matter core.

3.4.2 When anisotropy is not recovered

We have seen in Fig. 2 that a number of dwarf galaxies have constant stellar velocity anisotropies, whereas GRAVSPHERE recovers radially biased values (e.g. 5, 18, 21). We now wish to establish why this occurs and the effect it has on the recovery of the mass profile.

We quantify the success with which GRAVSPHERE recovers the anisotropy profile by computing the fraction of the area covered by the blue shaded bands in Fig. 2 that overlaps with the 68 per cent confidence limits returned by PYGRAVSPHERE. We will refer to this quantity as $\delta\beta$.

In Fig. 6 we show the quality of fit of the best model to

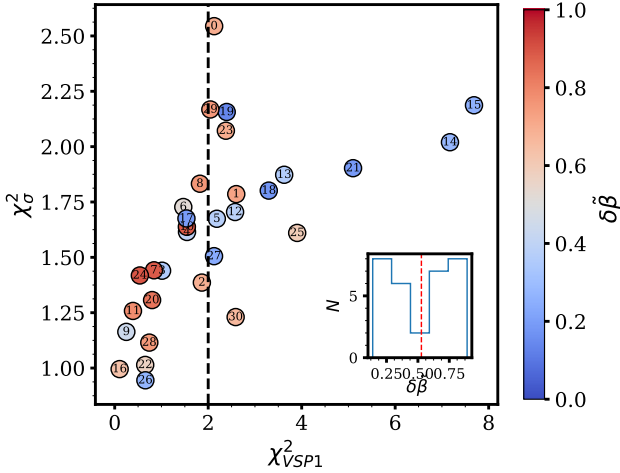


Figure 6. The value of χ^2 , divided by the number of data points, of the median model for the projected velocity dispersion, χ^2_σ , as a function of χ^2 of the first virial shape parameter, χ^2_{VSP1} . The points are coloured to represent the fraction of the anisotropy profile that has been successfully recovered, $\delta\beta$, as described in Section 3.4.2. The black dashed line shows our threshold χ^2_{VSP1} value, separating dwarfs with well and poorly recovered anisotropy profiles. The inset displays a histogram of $\delta\beta$. The red dashed line is the cut we make to differentiate between well and poorly recovered anisotropy profiles.

the line-of-sight velocity dispersion data, quantified by a χ^2 value, and the χ^2 for the first virial shape parameter. We take the best model to be the median value of the MCMC fits. For the velocity dispersion, we show the χ^2 divided by the number of kinematic data points. We colour the points by the quality of anisotropy recovery, $\delta\beta$.

A correlation between the two quantities is evident in Fig. 6. Outliers correspond to highly aspherical objects (0, 1, 25, 29, 30), with those viewed along the major axis showing a larger χ^2_σ (0, 23, 29) and others a particularly high χ^2_{VSP1} (1, 25, 30). Excluding especially aspherical objects, for each value of χ^2_σ , it is the models with poorer fits in VSP1 that typically have poor anisotropy profile recovery.

Is the best model fit to data effectively determined by VSP1? What causes the poor anisotropy recovery, leading to an underestimate in the masses recovered by GRAVSPHERE? To answer these questions we consider the GRAVSPHERE noVSP run. Galaxy 18 is a clear example where the anisotropy is not well recovered, leading to an underestimate of the enclosed mass. We select 1000 MCMC chains at random for this system and plot the anisotropy profiles proposed by EMCEE, coloured by the χ^2 of the four main terms in Equation 9. The results of this are shown in Fig. 7.

It can be seen that the anisotropy models output by PYGRAVSPHERE approximately fall into 4-5 distinct types. A number of models are a good match to the true anisotropy profile (black solid line); however, models that tend to radial anisotropy in the outer parts result in better values of χ^2 (black dashed line). Velocity dispersion data favours models that are more radial, while the surface brightness favours constant and tangential anisotropy models. If VSPs are not used, the best fit model is somewhere in the middle (black dotted line). When the virial shape parameters are included, it can be seen that VSP1 strongly disfavours constant and

tangential models, while VSP2 allows for a wide range of solutions. VSP2 is weighted by a factor of R^3 and is therefore more sensitive to the behaviour of $\langle v_{LOS}^4 \rangle$ in the outer regions. Since we marginalize over the behaviour of $\langle v_{LOS}^4 \rangle$ at large radii, this parameter has a greater error and thus permits a wider range of models. In effect, we can tell that VSP1’s preference for more radial models determined GRAVSPHERE’s result. We note that the virial shape parameters themselves are not devoid of the $M - \beta$ degeneracy and that their computation is sensitive to the extrapolation of $\langle v_{LOS}^4 \rangle$, which is extremely noisy due to lack of spherical symmetry in realistic systems and the discrete nature of the simulations. Other issues, such as particle contamination may play a role. Nevertheless, we have shown in Fig. 4 that GRAVSPHERE achieves a far more consistent performance than Jeans analyses with VSPs excluded (see the RMS values). Moreover, we have seen in Fig. 6 that poor anisotropy recovery may be predicted through the value of χ^2_{VSP1} , which is increased due to the disagreement between best fitting models for each of σ_{LOS} , $\Sigma(R)$, VSP1 and VSP2. We now investigate the effect that these poorly recovered anisotropy models have on the global GRAVSPHERE performance.

3.4.3 Effect of anisotropy recovery

In Fig. 8, we divide our sample of dwarfs into those which have well recovered anisotropy profiles, quantified by $\chi^2_{VSP1} < 2$, and those that do not. We can see that in cases where the anisotropy is not recovered, the masses are typically underestimated by up to 20 per cent (RMS = 0.16). Note however, that this is specifically due to the anisotropy models recovered by PYGRAVSPHERE being excessively radial. For galaxies with $\chi^2_{VSP1} < 2$ the enclosed mass estimates are overall unbiased, though the scatter is quite large. This is primarily due to SIDM galaxies 26 and 28, which are major axis projections.

3.5 The effect of tides

In this section we explore whether the mass profiles recovered by GRAVSPHERE are affected by tidal interactions. Dwarfs in our sample were selected to be satellites, which are susceptible to tidal stripping by their host galaxy. We have previously discussed Galaxy 18, which is an example of a dwarf where anisotropy is poorly recovered. Could this be attributed to tidal effects?

In the top left panel of Fig. 9 we plot the pericentre of the satellite orbits as a function of the dark matter mass lost since infall. We find the pericentres by interpolating the position of each dwarf with respect to its host with a cubic spline. This method may overestimate the pericentres (see Richings et al. 2018); however, for all of our dwarfs we see little difference between pericentres found through the linear and cubic splines. Moreover, the majority of the dwarfs have infall times of ~ 8 Gyr, such that typically 2-3 orbital periods are available for pericentre calculation, with snapshots having shorter temporal spacings at early times. We define the infall time as the snapshot at which the subhalo has its maximum dark matter mass. The points are coloured by the quality of anisotropy recovery, $\delta\beta$. As expected, the dwarfs with smaller pericentres tend to lose larger fraction

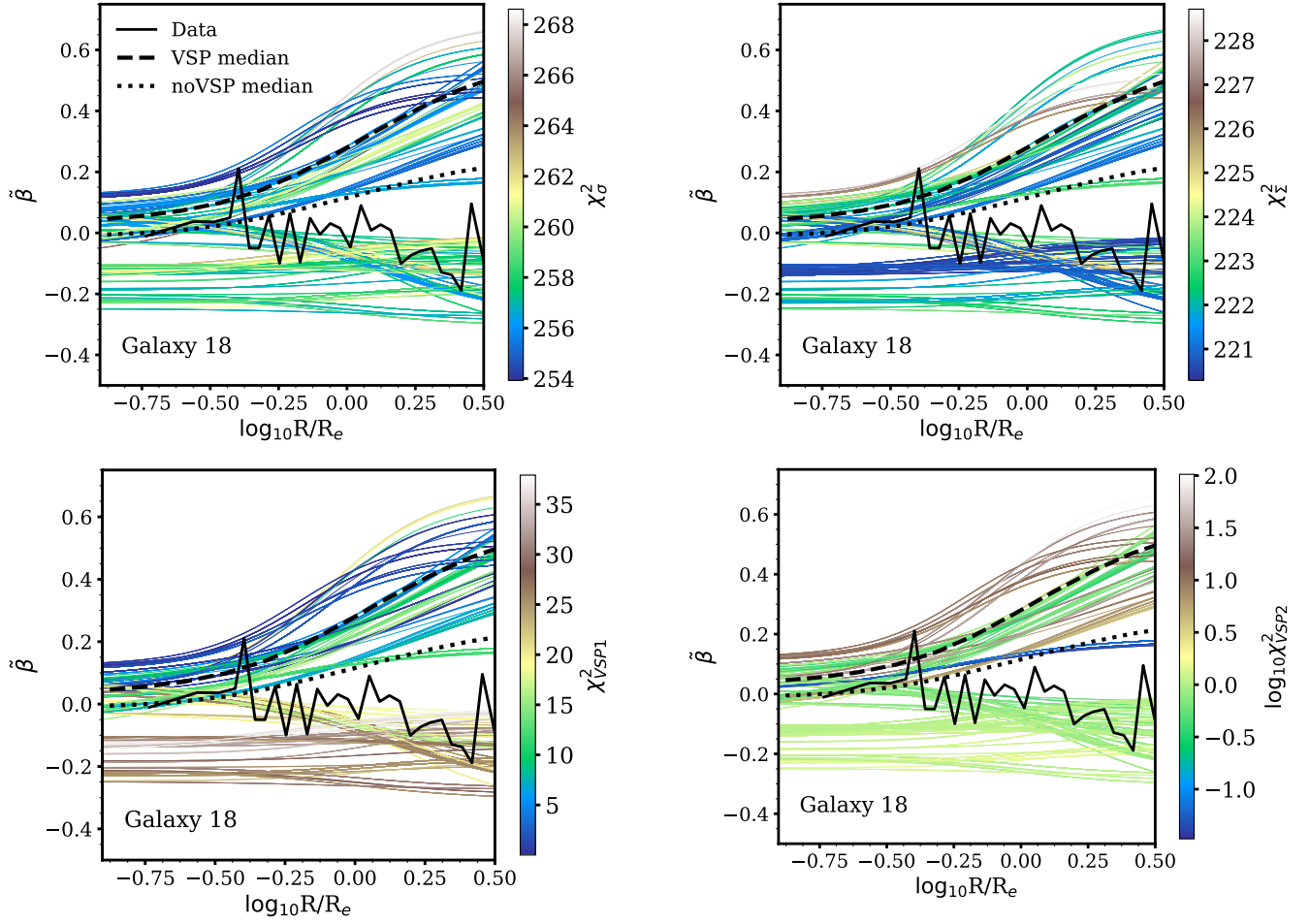


Figure 7. Random anisotropy profiles output in the noVSP MCMC run for Galaxy 18. The solid black line shows the mean anisotropy profile calculated from stellar particle data. The dashed black line shows the median model from the default GRAVSPHERE run and the dotted line shows the median model from the noVSP run. Across the four plots, the models are coloured by the χ^2 of four main components, as follows. *Top left*: projected velocity dispersion. *Top right*: surface brightness. *Bottom left*: VSP1. *Bottom right*: VSP2. Note the log-scale in the colour bar of this plot. The measurement of VSP2 requires extrapolation and marginalisation over the possible outer slopes of the fourth velocity moment and is strongly sensitive to the behaviour in the outer regions.

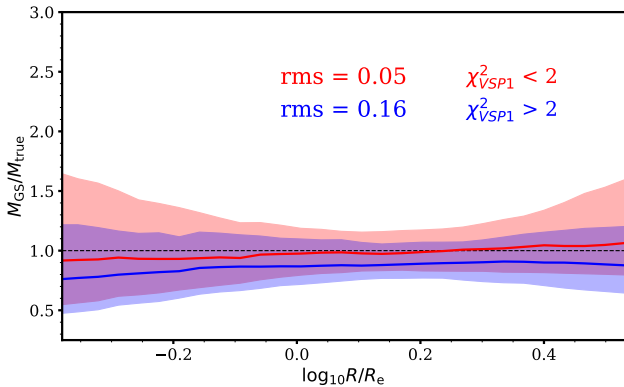


Figure 8. Mass profile recovery by the default GRAVSPHERE model for two sets of galaxies: those with $\chi^2_{VSP1} < 2$ (red) and those with $\chi^2_{VSP1} > 2$ (blue), where χ^2_{VSP1} is used as a tracer of how well the anisotropy is recovered.

of their mass. It is clear that Galaxy 18 is one of the most extreme cases of mass loss due to tides, with a pericentre of < 20 kpc and over 90 per cent of the original mass lost. Nevertheless, whilst the majority of galaxies with poor anisotropy recovery have been tidally stripped, no correlation is evident throughout the sample.

In the top right of Fig. 9 we show anisotropy gradients as a function of lost dark matter mass. We measure the anisotropy gradients between two points: mean stellar particle positions below and above the projected half-light radius. A clear trend is evident, whereby tides cause more tangential anisotropies in the outer parts of the galaxies. This is indeed the case in Galaxy 18, where the anisotropy profile becomes more tangential in the outer regions. This is due to the preferential stripping of the stars moving on radial orbits (Kravtsov et al. 2004). Once again, no trend is evident with the quality of anisotropy recovery by GRAVSPHERE.

We now split our sample of dwarfs into two groups: those that are expected to have been affected by tides more,

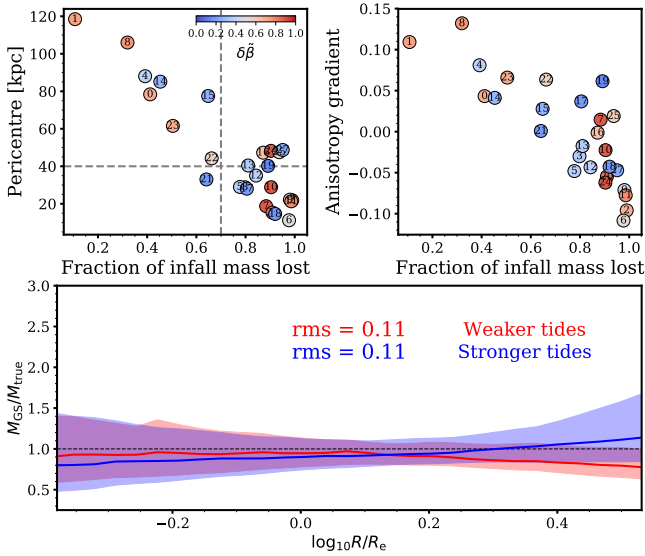


Figure 9. The effect of tides. *Top left:* the pericentre of the dwarf galaxy orbit as a function of the fraction of dark matter mass that has been lost since infall. The grey dashed lines show the selection of our subsample of dwarfs that are strongly affected by tides (bottom right corner). The points are coloured by the measure of anisotropy recovery by GRAVSPHERE, $\delta\beta$, with $\delta\beta \sim 1$ indicating good recovery. *Top right:* the radial change in anisotropy, quantified by a gradient measure below and above the half-light radius, as a function of dark matter mass lost through stripping. *Bottom:* the radial mass profile recovery for the subsample of dwarfs strongly affected by tides (pericentre < 40 kpc and lost mass \sim 70 per cent) and those less strongly affected.

and less severely. We define the severely stripped dwarfs as those with pericentric distance below 40 kpc and more than 70 per cent of stripped pre-infall mass (dashed grey lines in the top left of Fig. 9). In the bottom panel of Fig. 9 we show the radial mass profile recovery for the two groups. We exclude the pairs of dwarfs (1, 29), (8, 30) and SIDM dwarfs to remove asphericity and line-of-sight effects from this analysis, though our conclusions remain if those galaxies are included. There is a significant discrepancy in the accuracy of the enclosed mass recovery in the outermost regions of dwarfs, where the masses of the more tidally stripped sample tend to be overestimated. This discrepancy is expected, as the outer dark matter density slopes become steeper ($\gamma \sim 4$ compared to the maximum of $\gamma = 3$ permitted by the default PYGRAVSPHERE priors). In the inner regions, tides tend to lead to an underestimation of the enclosed mass. This result is more significant if we decrease the pericentric distance cut to select our subsamples. Nevertheless, this underestimation is no more than a 20 per cent effect.

Tidal stripping may be the cause of the poor mass profile recovery in Galaxy 18, although this does not affect dwarfs with comparable orbital parameters to the same extent.

3.6 Galaxy–halo offset

We have investigated the differences between the centre of mass of the stars and the dark matter for each dwarf in our sample. We found that offsets are present, with a typical

magnitude of 80 ± 35 pc for the CDM sample. For SIDM halos, however, the offsets are particularly extreme, with Galaxy 25(26) having an offset of 670 pc and Galaxy 27(28) having an offset of 710 pc. This is partly due to the difficulty in obtaining a centre of mass for density profiles with large cores, as well as lack of equilibrium. We repeated our analysis, comparing the mass profiles recovered by PYGRAVSPHERE to those computed directly from the simulation, now centering the “true” profiles at the centre-of-mass of the dark matter. We found no discernible differences from the results presented in Fig. 3. Moreover, separating the dwarfs into those with offsets > 80 pc and those with offsets < 80 pc, showed that the two groups are compatible within the 68 per cent confidence levels. We conclude that galaxy–halo offsets have no significant effect on the results presented in this work.

4 CONCLUSIONS

Dwarf spheroidals are some of the best objects to study the nature and distribution of dark matter due to their proximity and high dynamical mass-to-light ratios. In this work, we have explored the suitability of GRAVSPHERE (Read & Steger 2017), as well as other spherical Jeans analyses approaches, to determine the dark matter mass distribution in these galaxies.

First, we selected a sample of 31 dwarf galaxies from the APOSTLE suite of cosmological hydrodynamic simulations in Λ CDM and SIDM cosmologies. These simulated galaxies were chosen to resemble classical Local Group dwarfs like Fornax. We then applied GRAVSPHERE, with its standard set of priors, to each of these dwarfs. We found that within the key region inside the projected half-light radius, where dark matter cores form in some simulations (Navarro et al. 1996a; Tollet et al. 2016; Fitts et al. 2017; Oñorbe et al. 2015; Read et al. 2016; Pontzen & Governato 2012; Benítez-Llambay et al. 2019), the mass distributions are recovered within the 68 per cent confidence limits. Notable exceptions to this are the SIDM dwarfs included in our sample (which have inner cores), where the mass profiles are still recovered within the 95 per cent confidence limits.

We found that, for the whole sample, GRAVSPHERE returns unbiased mass profiles to within ~ 10 per cent accuracy (RMS = 0.06) along the radial range of $0.4R_e$ – $3R_e$, but with ~ 50 per cent scatter in the innermost regions and ~ 25 per cent scatter at the projected and the deprojected half-light radii; this is comparable to standard mass estimators (see the top panel of Fig. 3). In comparison to other Jeans methods, GRAVSPHERE achieves a more consistent performance across the radial range considered and, typically, has smaller scatter in the mass estimates (Fig. 4).

We note that our simulations suggest that Fornax-like dwarfs may have anisotropy profiles consistent with a constant value, $\beta = \beta_0$. In fact, assuming a constant β results in a performance comparable to GRAVSPHERE, with reduced scatter in the inner regions (see top right panel of Fig. 4).

We have explored the reasons for the scatter in the global performance of GRAVSPHERE. We found that objects viewed along their major axis typically have their masses recovered accurately (RMS = 0.05) compared to objects viewed along the minor (RMS = 0.14) and intermediate axes

(RMS = 0.13). This results in greater scatter in the accuracy of the enclosed mass estimates, which is more significant in the inner regions. For a sample of isolated dwarfs with asphericity $s \sim 0.7$, we find that asphericity, on average, leads to an underestimate of the enclosed mass. If Fornax has a sphericity of $s \sim 0.7$ and is viewed along the intermediate axis, GRAVSPHERE is expected to systematically underestimate its radial mass profile by ~ 25 per cent.

We have explored the effect of tides on the performance of GRAVSPHERE. We found that for severely stripped systems, the enclosed mass is underestimated by ~ 20 per cent at small radii. In the outer regions, where the outer dark matter slopes are typically steeper than those permitted by the default PYGRAVSPHERE priors, the masses are overestimated by ~ 10 per cent.

We explored the cases in which GRAVSPHERE underestimates the enclosed mass profile due to a biased estimate of velocity anisotropy. This occurs when the virial shape parameters force the MCMC algorithm towards a model that is inconsistent with the true value. Fourth order velocity moments are particularly sensitive to deviations from the standard Jeans equation assumptions of equilibrium and spherical symmetry as well as the noise present in the data. Nevertheless, we do find that the cases where the anisotropy is not well recovered manifest themselves through poor values of χ^2_{VSP1} (see Fig. 6). We suggest a $\chi^2_{VSP1} = 2$ cut to separate well and poorly recovered anisotropy profiles.

In conclusion, GRAVSPHERE is certainly a promising method for modelling dark matter in dwarf galaxies. We find a typical uncertainty on the enclosed mass is 50 per cent in the inner regions. For the density profiles, the uncertainty is only 30 per cent. Due to the spatial and mass resolution of our simulations we were only able to test GRAVSPHERE on regions outside ~ 380 pc, where the uncertainty of 30 per cent is too large to distinguish a cusp from a core based on the density profile; however, if this density uncertainty does not increase for regions near ~ 100 pc, it should be possible to separate core and cusp-like density profiles for Fornax-like dwarfs that have undergone complete core formation on the scale of the half-light radius, as described in Read et al. (2016), provided the central density has not been reduced by tides and the pre-infall halo mass is well constrained.

ACKNOWLEDGEMENTS

This work was supported by the Science and Technology Facilities Council (STFC) consolidated grant ST/P000541/1. AG acknowledges an STFC studentship grant ST/N50404X/1. CSF and SC acknowledges support by the European Research Council (ERC) through Advanced Investigator grant DMIDAS (GA 786910). This work used the DiRAC Data Centric system at Durham University, operated by the Institute for Computational Cosmology on behalf of the STFC DiRAC HPC Facility (www.dirac.ac.uk). This equipment was funded by BIS National E-infrastructure capital grant ST/K00042X/1, STFC capital grant ST/H008519/1, and STFC DiRAC Operations grant ST/K003267/1 and Durham University. DiRAC is part of the National E-Infrastructure. ADL is supported by the Australian Research Council (project Nr. FT160100250). This

work has benefited from the use on NUMPY, SCIPY and MATPLOTLIB.

REFERENCES

- Adams J. J., et al., 2014, *ApJ*, **789**, 63
 Albert A., et al., 2017, *ApJ*, **834**, 110
 Baes M., van Hese E., 2007, *A&A*, **471**, 419
 Barber C., Starkeburg E., Navarro J. F., McConnachie A. W., 2015, *MNRAS*, **447**, 1112
 Battaglia G., et al., 2006, *A&A*, **459**, 423
 Battaglia G., Helmi A., Tolstoy E., Irwin M., Hill V., Jablonka P., 2008, *ApJ*, **681**, L13
 Battaglia G., Helmi A., Breddels M., 2013, *New Astron. Rev.*, **57**, 52
 Benítez-Llambay A., Frenk C. S., Ludlow A. D., Navarro J. F., 2019, *MNRAS*, **488**, 2387
 Bett P., Eke V., Frenk C. S., Jenkins A., Helly J., Navarro J., 2007, *MNRAS*, **376**, 215
 Bonnivard V., Combet C., Maurin D., Walker M. G., 2015a, *MNRAS*, **446**, 3002
 Bonnivard V., et al., 2015b, *MNRAS*, **453**, 849
 Campbell D. J. R., et al., 2017, *MNRAS*, **469**, 2335
 Chabrier G., 2003, *PASP*, **115**, 763
 Charbonnier A., et al., 2011, *MNRAS*, **418**, 1526
 Cole D. R., Dehnen W., Read J. I., Wilkinson M. I., 2012, *MNRAS*, **426**, 601
 Contenta F., et al., 2018, *MNRAS*, **476**, 3124
 Crain R. A., et al., 2015, *MNRAS*, **450**, 1937
 Dolag K., Borgani S., Murante G., Springel V., 2009, *MNRAS*, **399**, 497
 Dutton A. A., Macciò A. V., 2014, *MNRAS*, **441**, 3359
 Elbert O. D., Bullock J. S., Garrison-Kimmel S., Rocha M., Oñorbe J., Peter A. H. G., 2015, *MNRAS*, **453**, 29
 Errani R., Peñarrubia J., Walker M. G., 2018, *MNRAS*, **481**, 5073
 Fattahi A., et al., 2016, *MNRAS*, **457**, 844
 Fitts A., et al., 2017, *MNRAS*, **471**, 3547
 Flores R. A., Primack J. R., 1994, *ApJ*, **427**, L1
 Foreman-Mackey D., Hogg D. W., Lang D., Goodman J., 2013, *PASP*, **125**, 306
 Fritz T. K., Battaglia G., Pawlowski M. S., Kallivayalil N., van der Marel R., Sohn S. T., Brook C., Besla G., 2018, *A&A*, **619**, A103
 Gaskins J. M., 2016, *Contemporary Physics*, **57**, 496
 Genina A., et al., 2018, *MNRAS*, **474**, 1398
 Goerdt T., Moore B., Read J. I., Stadel J., Zemp M., 2006, *MNRAS*, **368**, 1073
 González-Samaniego A., Bullock J. S., Boylan-Kolchin M., Fitts A., Elbert O. D., Hopkins P. F., Kereš D., Faucher-Giguère C.-A., 2017, *MNRAS*, **472**, 4786
 Górski K. M., Hivon E., Banday A. J., Wandelt B. D., Hansen F. K., Reinecke M., Bartelmann M., 2005, *ApJ*, **622**, 759
 Kravtsov A. V., Gnedin O. Y., Klypin A. A., 2004, *ApJ*, **609**, 482
 Lake G., 1990, *ApJ*, **356**, L43
 Ludlow A. D., Schaye J., Schaller M., Bower R., 2019a, arXiv e-prints, [p. arXiv:1908.05019](https://arxiv.org/abs/1908.05019)
 Ludlow A. D., Schaye J., Schaller M., Richings J., 2019b, *MNRAS*, **488**, L123
 Ludlow A. D., Schaye J., Bower R., 2019c, *MNRAS*, **488**, 3663
 McConnachie A. W., 2012, *AJ*, **144**, 4
 Merrifield M. R., Kent S. M., 1990, *AJ*, **99**, 1548
 Moore B., 1994, *Nature*, **370**, 629
 Morselli A., Consortium C., 2017, in 35th International Cosmic Ray Conference (ICRC2017). p. 921 ([arXiv:1709.01483](https://arxiv.org/abs/1709.01483))
 Navarro J. F., Eke V. R., Frenk C. S., 1996a, *MNRAS*, **283**, L72
 Navarro J. F., Frenk C. S., White S. D. M., 1996b, *ApJ*, **462**, 563
 Navarro J. F., Frenk C. S., White S. D. M., 1997, *ApJ*, **490**, 493

- Oñorbe J., Boylan-Kolchin M., Bullock J. S., Hopkins P. F., Kereš D., Faucher-Giguère C.-A., Quataert E., Murray N., 2015, *MNRAS*, **454**, 2092
- Oh S.-H., de Blok W. J. G., Walter F., Brinks E., Kennicutt Robert C. J., 2008, *AJ*, **136**, 2761
- Oh S.-H., et al., 2015, *AJ*, **149**, 180
- Orkney M. D. A., Read J. I., Pettis J. A., Gieles M., 2019, *MNRAS*, **488**, 2977
- Peñarrubia J., Navarro J. F., McConnachie A. W., Martin N. F., 2009, *ApJ*, **698**, 222
- Planck Collaboration et al., 2018, arXiv e-prints, p. arXiv:1807.06209
- Plummer H. C., 1911, *MNRAS*, **71**, 460
- Pontzen A., Governato F., 2012, *MNRAS*, **421**, 3464
- Power C., Navarro J. F., Jenkins A., Frenk C. S., White S. D. M., Springel V., Stadel J., Quinn T., 2003, *MNRAS*, **338**, 14
- Read J. I., Gilmore G., 2005, *MNRAS*, **356**, 107
- Read J. I., Steger P., 2017, *MNRAS*, **471**, 4541
- Read J. I., Wilkinson M. I., Evans N. W., Gilmore G., Kleyna J. T., 2006, *MNRAS*, **367**, 387
- Read J. I., Agertz O., Collins M. L. M., 2016, *MNRAS*, **459**, 2573
- Read J. I., Iorio G., Agertz O., Fraternali F., 2017, *MNRAS*, **467**, 2019
- Read J. I., Walker M. G., Steger P., 2018, *MNRAS*, **481**, 860
- Read J. I., Walker M. G., Steger P., 2019, *MNRAS*, **484**, 1401
- Richings J., et al., 2018, arXiv e-prints, p. arXiv:1811.12437
- Robertson A., Massey R., Eke V., 2017, *MNRAS*, **465**, 569
- Robertson A., et al., 2018, *MNRAS*, **476**, L20
- Sawala T., et al., 2016, *MNRAS*, **457**, 1931
- Schaye J., et al., 2015, *MNRAS*, **446**, 521
- Spergel D. N., Steinhardt P. J., 2000, *Physical Review Letters*, **84**, 3760
- Springel V., 2005, *MNRAS*, **364**, 1105
- Springel V., White S. D. M., Tormen G., Kauffmann G., 2001, *MNRAS*, **328**, 726
- Strigari L. E., 2018, *Reports on Progress in Physics*, **81**, 056901
- Strigari L. E., Bullock J. S., Kaplinghat M., Simon J. D., Geha M., Willman B., Walker M. G., 2008, *Nature*, **454**, 1096
- Strigari L. E., Frenk C. S., White S. D. M., 2010, *MNRAS*, **408**, 2364
- Tollet E., et al., 2016, *MNRAS*, **456**, 3542
- Ural U., Wilkinson M. I., Read J. I., Walker M. G., 2015, *Nature Communications*, **6**, 7599
- Walker M. G., Peñarrubia J., 2011, *ApJ*, **742**, 20
- Walker M. G., Mateo M., Olszewski E. W., Bernstein R., Wang X., Woodroffe M., 2006, *AJ*, **131**, 2114
- Walker M. G., Mateo M., Olszewski E. W., Peñarrubia J., Wyn Evans N., Gilmore G., 2009, *ApJ*, **704**, 1274
- Wolf J., Martinez G. D., Bullock J. S., Kaplinghat M., Geha M., Muñoz R. R., Simon J. D., Avedo F. F., 2010, *MNRAS*, **406**, 1220
- Zhao H., 1996, *MNRAS*, **278**, 488
- Zhu Q., Marinacci F., Maji M., Li Y., Springel V., Hernquist L., 2016, *MNRAS*, **458**, 1559
- de Blok W. J. G., 2010, *Advances in Astronomy*, **2010**, 789293
- de Boer T. J. L., et al., 2012, *A&A*, **544**, A73
- del Pino A., Aparicio A., Hidalgo S. L., Łokas E. L., 2017, *MNRAS*, **465**, 3708

APPENDIX A: CONVERGENCE CRITERIA AND GENERATING INITIAL POSITIONS

In this section we describe the effect of our choice of the initial positions of EMCEE walkers on the convergence of PYGRAVSPHERE’s results.

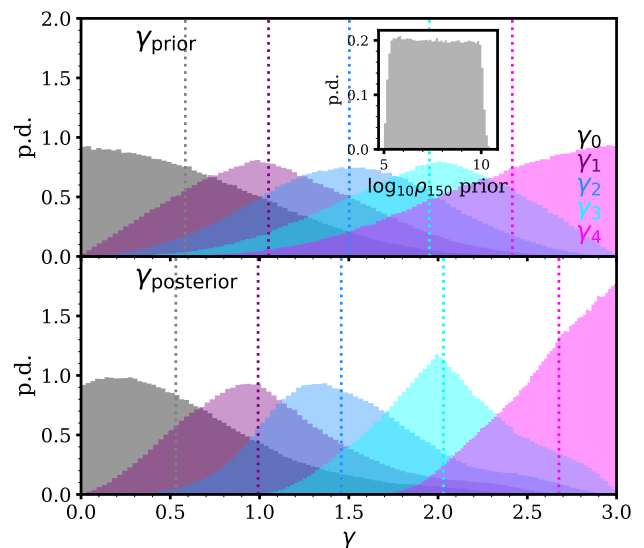


Figure A1. *Top:* effective priors on the logarithmic slopes γ_j . Each slope is identified by its colour. The inset shows priors on the density at 150 pc, assuming a 1 kpc half-light radius. *Bottom:* posterior distributions, collected from all dwarfs within our sample, weighted equally. The dotted lines are the medians of the distributions.

A1 Effective priors

As mentioned in the main text, we generate the initial positions through the selection of walkers that satisfy the condition of radial increase in power-law slopes γ_j and the constraint on smoothness $\Delta\gamma = 1$.

The top panel of Fig. A1 shows the effective priors on each slope. It is clear that these priors are not uniform as the selection of the slopes is not independent; however, the width of these distributions allows for a variety of density profiles. The inset shows the priors for the density at 150 pc, ρ_{150} . Despite the non-uniform nature of the γ_0 prior, when combined with a uniform prior on the scale density, ρ_0 , the resulting ρ_{150} prior is effectively uniform and is not biased towards more core or cusp-like values (Read et al. 2019).

The bottom panel of Fig. A1 suggests that the posteriors on γ are not completely determined by the priors. The prior and posterior distributions are offset, as seen from their median values, and their shapes are noticeably different. The γ_4 posterior is clearly pushing against the prior boundary, suggesting that a wider prior on this parameter is desirable.

A2 Convergence compared to previous implementations

Previous implementations of GRAVSPHERE have used initial positions of the walkers for the broken power law slopes γ_j that are completely uniform. This results in a large number of EMCEE walkers starting off in regions of infinitely negative log-likelihood. This is because these walkers do not satisfy the constraints for monotonically increasing values of γ_j . We will refer to these as “dead walkers”. Eventually, some of these climb out and explore the posterior distribution, but not all, and this can take many iterations. In Read & Steger

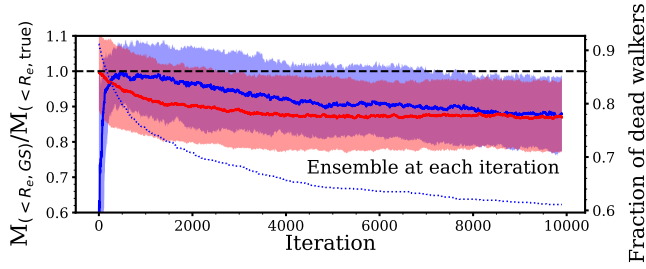


Figure A2. The convergence of mass within the half-light radius, expressed as an accuracy compared to the true value, for two different prior selection methods. Priors that are generated completely uniformly are shown in solid blue, and those selected in a uniform, yet conditional, fashion (such that all priors satisfy the monotonic increase in the values of γ_j) are shown in red. The shaded bands represent 68 per cent confidence limits. The blue dotted line shows the fraction of “dead walkers” (those stuck in the infinitely negative log likelihood space), when using fully uniform priors.

(2017), the chains were run for 5000 iterations, with the last 2500 used for analysis. In Fig. A2 we compare this method to one employed in this work.

We pick Galaxy 4 as our representative example and we select the mass within the half-light radius, $M(< R_e)$, as a quantity for which we wish to establish convergence. Fig. A2 shows the median value of accuracy, $M(< R_e)/M_{\text{true}}$, and the 68 per cent CLs for *each* walker iteration using the original GRAVSPHERE’s method for generating initial positions (blue) and the initial positions generated using the method described in this work (red). The blue dotted line shows the fraction of dead walkers remaining after each iteration when using the original GRAVSPHERE method (right vertical axis).

It can be seen that our new method reaches convergence after $\sim 5 \times 10^3$ iterations, whereas the original method requires ~ 500 iterations to get out of the low log-likelihood regions and, in fact, does not reach the converged distribution until after $\sim 9 \times 10^3$ MCMC iterations. The chains start off with over 90 per cent dead walkers. This percentage drops to ~ 60 per cent near 10^4 iterations and can be seen to decrease slowly. We conclude that our new method of initial position selection allows for faster chain convergence and an efficient walker exploitation.

This paper has been typeset from a $\text{\TeX}/\text{\LaTeX}$ file prepared by the author.